Efficient Water Area Classification Using Radarsat-1 SAR Imagery in a High Relief Mountainous Environment

Yeong-Sun Song, Hong-Gyoo Sohn, and Choung-Hwan Park

Abstract

It is important to determine quickly the extent of flooding during extreme cases. Even though SAR imagery with its own energy sources is highly applicable to flood monitoring owing to its sensitivity to the water area, topographic effects caused by local terrain relief must be carefully considered before the actual classification process. Since backscattering coefficients of the shadow area in high relief regions are very similar to those of the water area, it is essential to regard these areas before and after the classification procedure, although the process is a difficult and time-consuming task. In this study, efficient and economical methods for water area classification during floods in mountainous area are described. We tested five different cases using various synthetic aperture radar (SAR) image processing techniques, texture measures, and terrain shape information such as elevation and slope. The case whereby the SAR image was classified with the local slope information exhibited the best result for water area classification, even in small streams of different elevation categories. Consequently in mountainous areas, the combination of a SAR image and local slope information was the most appropriate method in estimating flooded areas.

Introduction

Synthetic Aperture Radar (SAR), an active sensor, transmits pulses of microwave and detects echo, which carries information about the surface. Due to relatively long wavelengths in microwave, radar signals are capable of penetrating clouds in the atmosphere and are independent of sunlight. These characteristics of SAR are particularly useful in monitoring floods over large areas, while accurate flood mapping using other methods is difficult since hydrologic instrument data and optical imagery are limited. The accurate delineation of flood extent provides important information that can help guide management decisions and provide necessary data for flood mapping applications. Although SAR data have been widely applied to these kinds of situations, some problems need to be solved before they can be put to actual use.

Numerous investigations have been carried out to examine the capabilities of SAR sensors for wetland mapping and monitoring flooded areas (Imhoff *et al.*, 1987; Hess *et al.*, 1995; Pope *et al.*, 1997; Brakenridge *et al.*, 1998; Miranda and Fonseca, 1998; Alsdoforf *et al.*, 2001; Townsend, 2001; Wickel and Jackson, 2001; Horritt *et al.*, 2002). In previous works, since most of the areas studied involved flat terrain that did not cause serious radiometric distortions, it was relatively easy to delineate water extent. The works of Giacomelli *et al.* (1995), Birkett (1999), Liu *et al.* (2002), and Costa (2004) used SAR images to extract water areas through histogram analysis by setting the pre-defined threshold value. The threshold value, however, practically varies in every case, and it is not an easy to set the accurate threshold value to distinguish between water areas and non-water areas. In mountainous areas, the pre-defined threshold method may mistakenly classify non-water area into water area due to the more serious topographic effects caused by high terrain relief.

The radiometric distortions depend strongly on the terrain and increase significantly in mountainous areas, in which the distortions should be corrected by a backscatter model for better classification results. Several studies have examined the influence of terrain relief on SAR images and proposed various correction procedures. van Zyl *et al.* (1993) and Ulander (1996) considered the inclination of the backscattering surface in azimuth and in range, in order to achieve more accurate radiometric corrections of topographic effects on SAR images. van Zyl *et al.* (1993) used the local incidence angle of the surface as a projection factor, while Ulander (1996) used the smallest angle between the surface normal and the image. Teillet *et al.* (1985) made use of an empirical cosine-based backscatter model, while Rauste (1989) examined the effect of topography on the imaging geometry and set up an empirical model of the backscatter variations.

While an accurate Digital Elevation Model (DEM) is available, it is possible to correct topographic effects. However, this requires an enormous amount of time and complicated procedures. In very rugged terrain areas such as the Korean peninsula, new errors could manifest while removing topographic effects due to the uncertainties in the accuracy of elevation (Goering *et al.*, 1995; Goyal *et al.*, 1998; Sun *et al.*, 2001; Bernier *et al.*, 2002). Especially for radar shadows, since there is no signal to be normalized and no improvement can be expected, SAR images have limited use for flood monitoring in high terrain relief regions.

School of Civil and Environmental Engineering, Yonsei University, 134 Shinchon-Dong Seodaemun-Gu, Seoul, 120-749, Korea (sohn1@yonsei.ac.kr).

A SAR image alone is rather hard to apply in flood event analysis due to speckles noise, poor visual interpretation, and the single radar tonal channel. Previous studies have shown that tonal classification of a single-date SAR image might produce poor classification results (Aschbacher *et al.*, 1995; Wang *et al.*, 1998). Additional data sets such as optical satellite images, texture information referring to the spatial distribution of tonal variation, and terrain information can help improve the accuracy of classification results. The water area classification of SAR images, in particular, could be significantly improved by using multi-date and multi-sensor images (Shang, 1996; Wang *et al.*, 1998; Sokol *et al.*, 2000; Milne *et al.*, 2000; Töyrä, 2002). However, multi-date and multi-sensor images are not always available.

The texture information derived from a SAR image has been a very valuable characteristic for discriminating among different land-cover types. Texture measures computed from gray-level co-occurrence matrix (GLCM) have been widely used for land-cover classification with optical and radar data (Pultz and Brown, 1987; Marceau *et al.*, 1990; Kurvonen and Hallikainen, 1999; Treitz *et al.*, 2000). Some described that texture information may be more useful than the image tone itself for interpreting a SAR image (Ulaby *et al.*, 1986).

Terrain information can also help improve the accuracy of SAR image classification used as an additional source. There are few existing studies that combine SAR images with terrain information for land-cover mapping. Peng *et al.* (2003) mapped land-cover in mountainous areas of southern Argentina using both the texture analysis of radar imagery and a DEM generated from the same data source of a radar stereo pair. Their study showed that DEM information was useful for land-cover mapping in mountainous areas.

In this study, we apply SAR imagery with additional information derived from the SAR image itself or from different sources such as DEM and Digital Surface Model (DSM) in flood mapping. Various combinations of SAR imagery with GLCM texture measures, DSM and/or DEM and the best and most efficient among all combination to classify the water area were selected. In this study, water area refers to the flooded area above normal plus normal water area during ordinary times.

The accuracy of water area classification was estimated using visual interpretation analysis, the water area extraction ratio on the basis of slope, and an error matrix constructed using land-use map and the Annual Disaster Report of 1998 provided by the Korean National Disaster and Prevention and Countermeasure Headquarters (KNDPCH).

As a result of various tests, the case when the SAR image combined with the local slope information processed by two iterations of MIN filter with 3×3 window size gave the best performance in terms of water area estimation during flooding, even in small streams with different elevation categories. Consequently in the mountainous areas, the combination of SAR image with the local slope information exhibited the best classification result in terms of time and efficiency.

Study Area and Data Description

Flood-related disasters have been most serious and frequent in Korea, causing substantial suffering, severe losses of life, and economic damage. In 1998, two typhoons, Yanni and Penny, tragically passed over the middle province of Korean peninsula, and among the hardest hit areas most suffered areas were the residential and agricultural areas of Ok-Chun and Bo-Eun City. Penny visited the Korean peninsula

between 11–12 August 1998 and caused about 400 mm/day precipitation on 12 August alone. The study area can be characterized as a narrow and mountainous region, so flash flood history has been frequently recorded. The elevation ranges from 28 to 830 m, indicating high relief areas, and the maximum local slope is up to 64°. A single-date RADARSAT-1 SAR path image, acquired on 12 August 1998, with HH polarization and standard beam mode, is used for this study. Figure 1 shows RADARSAT-1 SAR amplitude image and the location of the study area.

The high probable water areas usually present the characteristics of relatively lower elevation than the surroundings, lower slope due to water flow, and appear lower radar backscatter coefficients in a SAR image. Terrain information can be used to improve the classification, and the most commonly used information is DEM. DEM can be generated by stereo images using the space intersection method, or lidar data, SAR interferogram, and paper or digital topographic maps could be possible sources for DEM. In this study, DEM was generated from 1:5 000 scale digital topographic maps provided by the Korean National Geographic Information Institute (KNGII). The DSM was also derived from the DEM and has the same spacing as that of DEM for further analysis. Detailed description of DEM and DSM will be provided in the later sections.

Water Area Classification

In this study, a RADARSAT-1 SAR image and additional data that were relatively inexpensive and easy to obtain, process, and analyze were used for water area classification during a flooding event. Figure 2 depicts the schematic diagram of the whole processing step used in this study. As shown in Figure 2, we tested five different cases for water area classification applicable to high relief mountainous areas; (a) preprocessed SAR image, (b) GLCM texture information acquired from preprocessed SAR image, (c) preprocessed SAR image combined with radiometric slope correction, (d) preprocessed SAR image with DEM, and (e) preprocessed SAR image with DSM. Here, preprocessing refers to general SAR image processing steps such as radiometric and geometric correction. The radiometric correction step involves the calculation of radar backscatter coefficients, the antenna pattern compensation, and the speckle noise reduction. The preprocessing step does not include the radiometric slope correction of topographic effect caused by the local terrain relief. The rigorous geometric correction developed in our research group (Sohn *et al.*, 2005) was also performed as a preprocessing step using ground control points (GCPs) and a DEM.

Due to the physical characteristics of the water area, the extent of water during a flooding is also greatly affected by the local terrain. Therefore, we expected that local terrain information could be a useful tool for improving the accuracy of water area classification in the mountainous area. Terrain information such as aspect, flow accumulation, and watershed might be good additional sources of data, but our tests showed that these details could not improve the accuracy of our results, so they were not discussed in this study. Since the result from RADARSAT-1 SAR image combined with both DEM and DSM were so similar to those of case 4 (DEM only) in Figure 2, this was also excluded from further consideration.

Special attention is needed in the case when DSM was used as additional information. It is assumed that the probabilities of water area are high in the lower slope condition. When the water area is suddenly extended by a
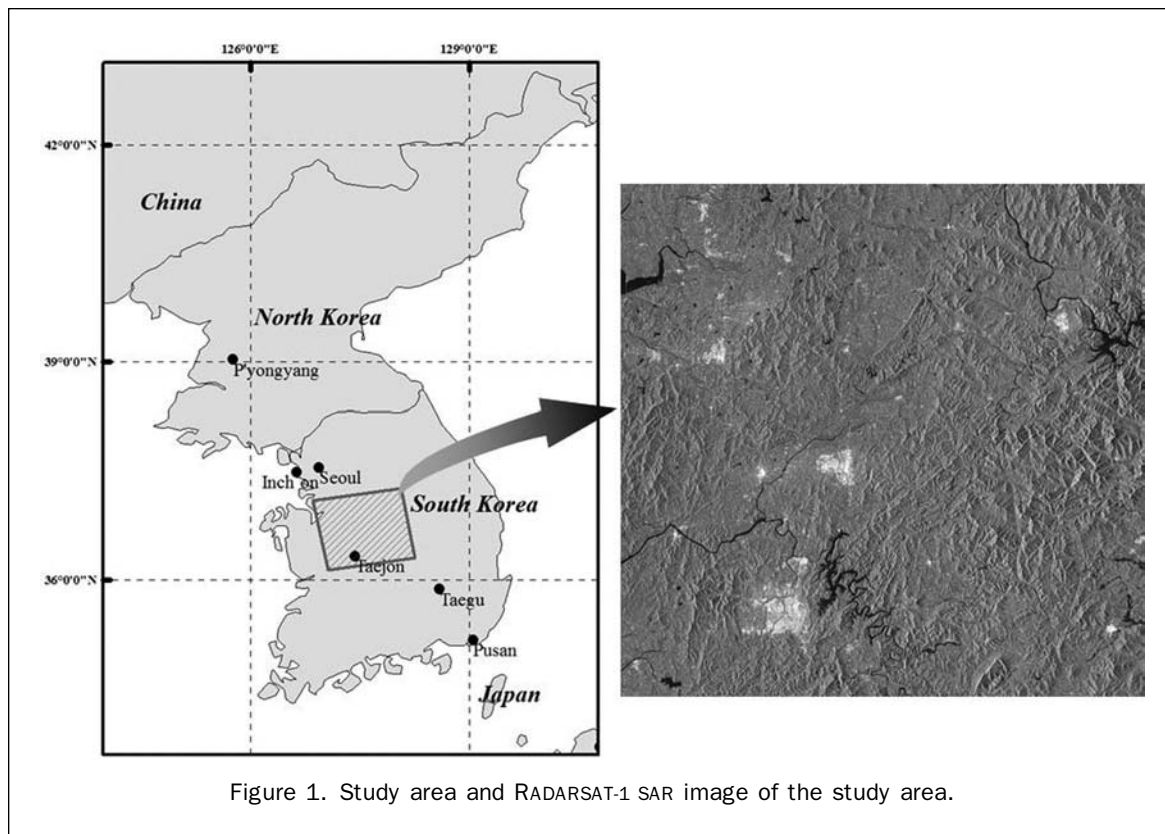
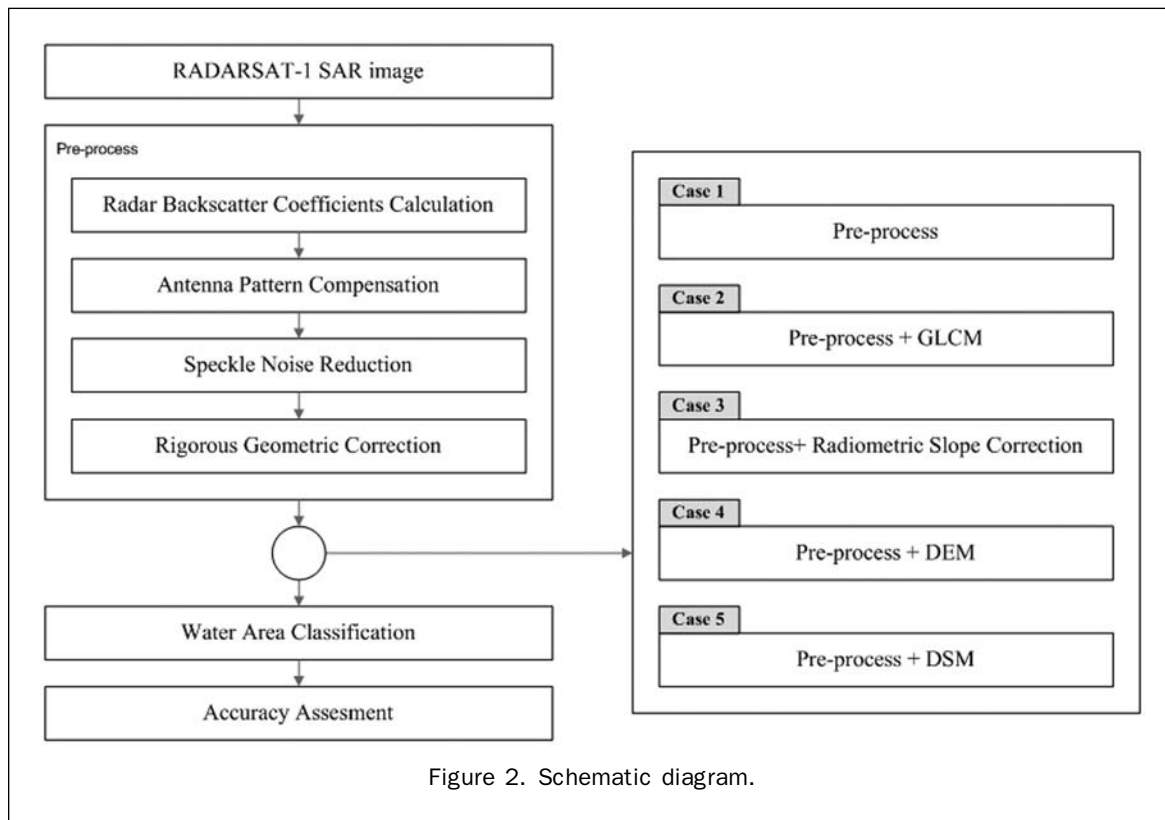Figure 1. Study area and RADARSAT-1 SAR image of the study area.

Figure 2. Schematic diagram.

flash flood, this assumption may not be true any more. This means that there exists a high probability of water area at the boundary between the water area during ordinary days and the bank. To resolve the problem, the MIN filter that selects the smallest value within the filter window was applied to the DSM.

The supervised maximum likelihood method was used to classify the water area in all cases mentioned in Figure 2. The rationale of using this approach here is that the preprocessing through spatial filtering not only reduced the variance, but also the skew of the distribution to an extent that a Gaussian distribution applies (Lee, 1981; Giesen, 2000). The accuracies of each classification result were checked using three different methods: visual inspection, an error matrix, and the water area extraction ratio.

Preprocessing Procedure

The first preprocessing step is converting digital number (DN) to backscatter coefficients. The radar backscatter coefficients, σ^0, were calculated for the radiometric correction instead of conventional 16-bit DN (digital numbers) values. The radar brightness, β^0, should be informed to calculate to get σ^0 and calculated by Equation 1:

$$\beta_j^0 = 10 \times \log_{10}\left[(DN_j^2 + A_3)/A_{2j}\right] \tag{1}$$

where, A_{2j} is the scaling gain value of jth pixel toward a slant range direction, determined by interpolating gain values provided from the image header file. A_3 is a fixed offset and DN_j refers to the digital number that represents the magnitude of jth pixel from the start line of a range line in the image data. σ_0, then, can be obtained as follows (see Equation 2), and its unit is in dB:

$$\sigma_j^0 = \beta_j^0 + 10 \log_{10}(\sin I_j) \tag{2}$$

where, I_j is the incidence angle of jth range pixel and could be calculated from Equation 3 below:

$$I_j = \cos^{-1}\left[\frac{(h^2 - r_j^2 + 2 \cdot R \cdot h)}{2 \cdot r_j \cdot R}\right] \tag{3}$$

where, R is the earth radius, h is the orbit altitude for the image, and r_j is the slant range of jth pixel. Since the ground range image is used in this study, the Equation 4 is used to convert from the ground range to the slant range:

$$r_j = a + j \cdot dRg \cdot b + (j \cdot dRg)^2 \cdot c + (j \cdot dRg)^3 \cdot d$$
$$+ (j \cdot dRg)^4 \cdot e + (j \cdot dRg)^5 \cdot f \tag{4}$$

where $a, b, c, d, e,$ and f are the conversion coefficients from a ground range to a slant range, and dRg represents the pixel spacing.

Since the antenna pattern causes different pixel values for the same or similar objects in RADARSAT-1 SAR image and the radiation distortion occurs along the range direction, the central part of the radar image is brightest, and its brightness gradually decreases from the central part to its two sides (Liu et al., 2002). For certain SAR geometries (e.g., SIR-C, wide swath SCANSAR), the local terrain height should also be considered during this correction. However, for single-beam RADARSAT-1 scenes, the high altitude of the satellite together with the relatively small range of incidence angles and the flatness of the antenna pattern within a single beam swath reduces the magnitude of such radiometric errors to one or two dB (Holecz et al., 1995). In this study, the second polynomial method was applied to compensate for the above.

The presence of speckle in an image reduces the detect ability of ground targets, obscures the spatial patterns of surface features, and decreases the accuracy of automated image classification (Sheng and Xia, 1996). Typical noise reduction filters, such as the moving average or the median filter, are not well suited for preserving edges. Zaman and others (1993) summarized the evaluation of several filters with respect to the edge preservation in single-look and multi-look SAR images and recommended the Lee-sigma filter. In this study, a Lee-sigma filter with a window size of 3×3 was applied twice for better accuracy.

Rigorous geometric correction is essential for the interpretation of SAR images of high relief areas to perform meaningful multi-source analysis using images acquired with different geometries. The main consideration with geometric correction is to find the slant range and azimuth coordinates in the SAR image of object points on the ground range. The fundamental equations to relate the ground and image coordinates are the range and Doppler equation (Curlander, 1982). In the geometric correction process, it is critical to estimate the satellite orbit parameters, but the RADARSAT-1 satellite had often provided inaccurate platform positional data. Substantial refinement of the orbit geometry using control points was required. A total of 20 GCPs were selected from 1:5 000 Korean digital topographic maps having horizontal and vertical accuracy of about 2 m, and were used to refine the satellite orbit parameters. The RADARSAT-1 SAR image was then transformed into map geometry, the Transverse Mercator coordinate system based on Bessel 1841 ellipsoid, using backward geometric correction technique (Sohn et al., 2005) and a DEM generated from the 1:5 000 Korean digital topographic maps of the study area.

Radiometric Slope Correction

The topographic effect depends on terrain relief of the target area and increases radiometric distortions. The local slope can cause the actual back scattering to be different from that calculated using the flat Earth assumption. This distortion can be corrected by a high-resolution DEM, but it is time-consuming and difficult to apply in rugged terrain. van Zyl (1993) proposed the radiometric slope correction of the topographic effects using a DEM. We applied his approach, which considers the local incidence angle of the surface, to the SAR image. According to van Zyl (1993), the power of received waves from the scattering area, A, is represented by Equation 5:

$$P_r = \frac{P_t \lambda^2 G_t(\gamma) G_r(\gamma)}{(4\pi)^3 R^4} \sigma^0 A \tag{5}$$

where P_t is the transmitted power, λ is the radar wavelength, R is the distance to the scattering area, γ is the radar look angle, $G_t(\gamma)$ and $G_r(\gamma)$ are the transmit and receive antenna gains at look angle γ respectively, and σ^0 is the normalized radar cross section for area A.

A is defined as Equation 6, when the ground is flat without terrain relief or spherical Earth:

$$A = \frac{\delta_r \delta_a}{\sin(\eta)} \tag{6}$$

where η is the incidence angle, and δ_r and δ_a are the slant range and azimuth pixel spacing, respectively. In reality, the scattering area of the non-flat terrain A' varies according to the ground slope and the azimuth direction when the image is acquired:

$$A' = \frac{\delta_r}{\sin(\eta - \varphi_r)} \frac{\delta_a}{\cos(\varphi_a)} \tag{7}$$

where φ_r is the tilt of the surface in the range direction, and φ_a is the tilt of the surface in the azimuth direction. Therefore, the difference introduced by using Equation 6 instead of Equation 7 is the value of the ratio A/A'. Figure 3 illustrates the geometry of SAR signal scattering surface by local terrain relief. Figure 4 represents the incidence angle
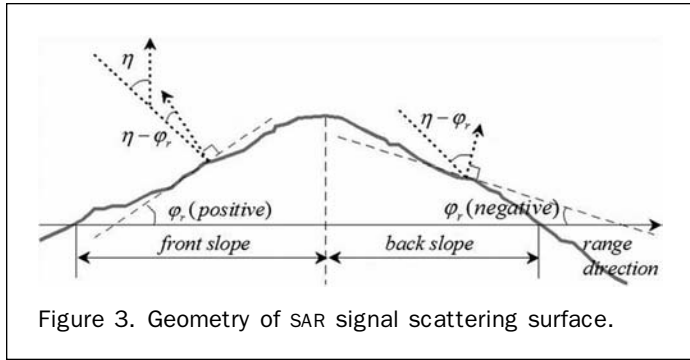
Figure 3. Geometry of SAR signal scattering surface.

map (η in Equation 6) and local incidence angle map ($\eta - \varphi_r$ in Equation 7) for radiometric slope correction estimated from the DEM.

GLCM Texture Measures

The GLCM is a two-dimensional array that provides the co-occurrence probability of pairs of gray-level pixels within a local window (Haralick *et al.*, 1973). Four parameters (window size, inter pixel angle, inter pixel distance, and quantization level) need to be considered when generating a GLCM. Haralick *et al.* (1973) defined 13 texture measures to be computed from the GLCM, and the seven GLCM texture measures were commonly used (Arzandeh and Wang, 2002). These are the homogeneity, the contrast, the mean, the variance, the entropy, the angular moment, and the correlation. The study showed that the accuracies increase remarkably when the number of texture channels increases from one to three. Adding the fourth texture did not improve the best results of three-texture combinations but did improve the best results of three-texture combinations that had lower accuracy. The relationship between window size and classification accuracy was positive, and the accuracies of classification increase with increasing window size until it reached the optimum size at 17 × 17 for various classification classes.

Water areas with larger sizes and smoother texture however, tend to exhibit lower accuracy when a window size increases. If the window size is too large, the misclassification seemed to have occurred in the borders of the water area. Also, excessively large windows tend to interfere with determination of small streams that have linear shapes. The window size and the combination of texture measures have been considered as two important factors that affect water area classification results using texture channels. To determine which combinations of texture measures produce better results at a certain window size, we performed several experiments
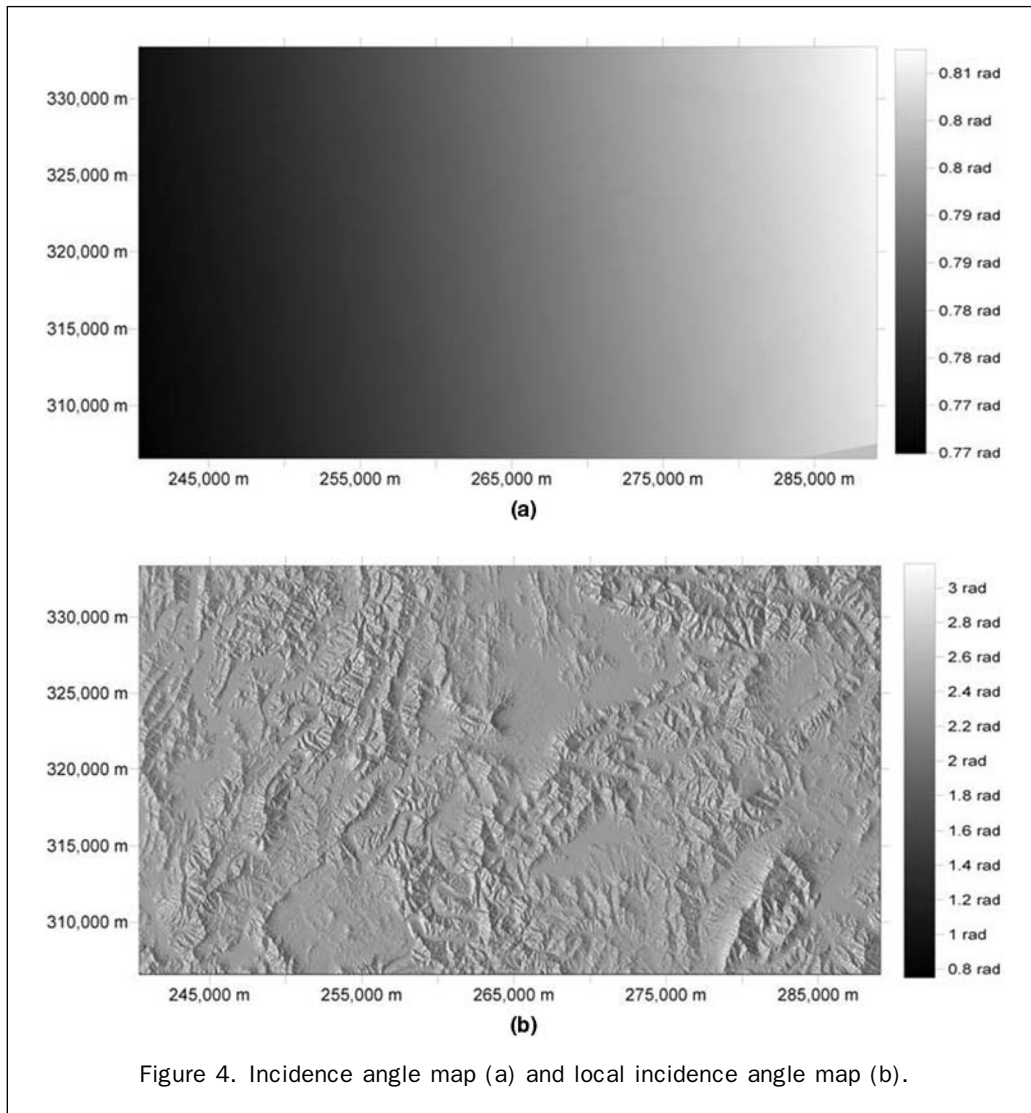

Figure 4. Incidence angle map (a) and local incidence angle map (b).

on various combinations of texture measures at different window sizes. The final three texture information selected are the mean, the contrast and the variance at a window size of 3 × 3 for water area classification. Figure 5 shows the mean, the variance, and the contrast texture measures generated from the preprocessed image.

Terrain Information

The overall accuracy of the 1:5 000 scale digital topographic map compiled photogrammetric method from 1:20 000 scale aerial photos are about 2 m horizontally and vertically. The spatial resolution of the DEM used in this study is 20 m. KNGII has generated several scale digital topographic maps that cover the Korean peninsula and these digital maps have been a good source of generating a DEM. Those maps are composed of several layers according to the ground object type, and the layers that contained three-dimensional

Figure 5. GLCM texture measures: (a) mean, (b) variance and (c) contrast.

coordinates were only selected to generate a DEM. These selected layers were used to construct the triangulated irregular network (TIN), which were then resampled to a 20 m grid format using Kriging algorithm. To ensure the quality of the DEM, we tested and searched any possible errors that need to be eliminated, and the final product of DEM is illustrated in Figure 6.

The DSM was calculated from the DEM and has the same pixel spacing as that of the DEM. Since the window size and the number of iterations are critical factors for the final result, we performed experiments on various numbers of iteration at different window sizes. Consequently, the MIN filter with two iterations and with widow size of 3 × 3 applied to the DSM to compensate for water boundary expansion caused by a flash flood. Figure 7 illustrates the result of the DSM before and after the MIN filter was applied. The dark areas represent the lower slope area and light areas refer to the higher slope area.

Water Area Classification

Plate 1 illustrates the images used for classifying each case in Figure 2. Each processed image has 20 m spatial resolution, which is the same as that of the generated DEM. The geometric accuracy of RADARSAT-1 SAR image was checked using 16 checkpoints. The results were 1.5 pixels for range direction and 1.8 pixels for azimuth direction, respectively. The image after the preprocessed procedure is not 16-bit DN values but dB values.

Plate 1a represents the preprocessed image. The calculated backscatter coefficients range from approximately −24.2 to 6.7 dB and water areas usually have low dB values around −20 dB. Plate 1b is a false color composite image combining three textures with mean as red, contrast as blue, and variance as the green band. Plate 1c represents the topographic effect corrected image cased by local terrain relief applied on the preprocessed image. For the study area, the radiometric distortion caused by topographic effect was corrected up to 6 dB. In Plate 1d, the preprocessed image was combined with the DEM for regarding terrain elevation. Finally, Plate 1e combined the preprocessed image and the DSM instead of the DEM. For the cases that combine SAR image with terrain information, the SAR image was assigned to a green band, the DEM and DSM to a red band, and a blank layer that has constant value to a blue band, respectively.

The supervised classification of the maximum likelihood was performed with 22 training sites. The training sites for 12 water and 10 non-water areas were carefully selected over an entire image. Since this study was focused
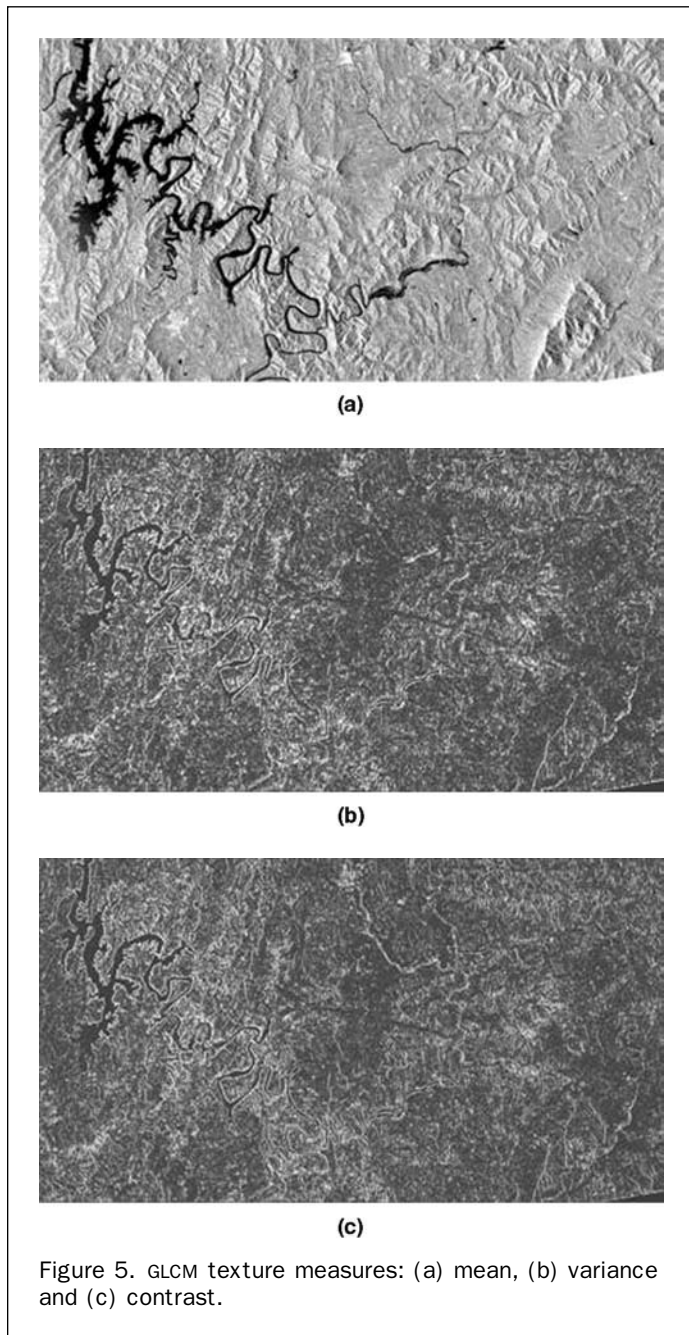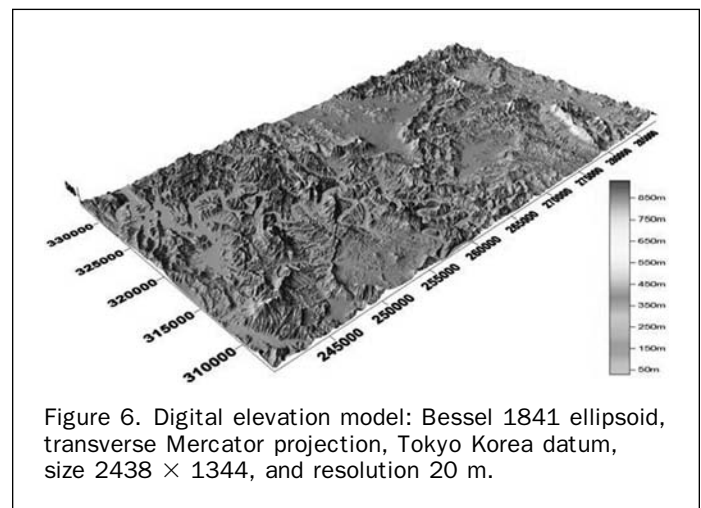

Figure 6. Digital elevation model: Bessel 1841 ellipsoid, transverse Mercator projection, Tokyo Korea datum, size 2438 × 1344, and resolution 20 m.
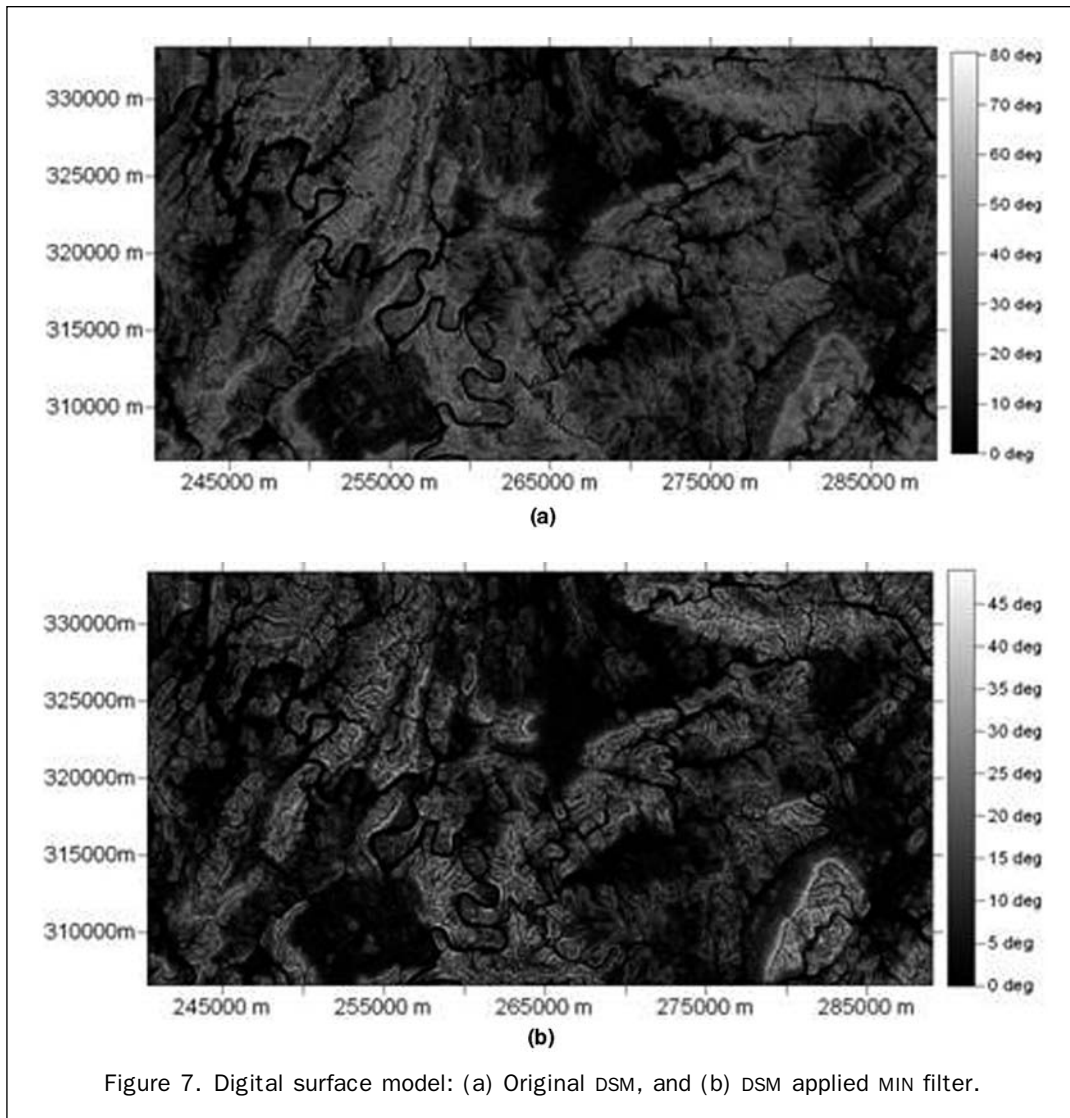
Figure 7. Digital surface model: (a) Original DSM, and (b) DSM applied MIN filter.

on identifying water and non-water areas in various elevations, training sites for water areas accumulated in various terrain areas were carefully selected over the region. Table 1 shows characteristics of the training site used for image classification. The results of supervised maximum likelihood classification for each case are shown in Figure 8.

Analysis of Classification Results

The reference data used for checking the accuracy of our results were land use map and the Annual Disaster Report 98 of the KNDPCH. We also manually generated the ground truth of region of interest (ROI) from the reference data to check the results and constructed an error matrix accordingly (Table 2).

As illustrated in Table 2, the overall accuracy of all cases exceeded 95 percent and case 5 showed the highest accuracy of 99.36 percent. The kappa coefficient results ranged from 0.89 to 0.98, and case 5 showed the highest kappa coefficient, 0.98. Although the accuracy of case 4 was very similar to that of case 5, the classification results were drastically different. Detailed discussions on all cases are as follows.

The dominant classification errors of case 1 were the errors caused by a severe topographic effect such as shadow regions where the high relief areas lied. The northwestern section, marked region *A* in Figure 8a, marked region *B* in Figure 8a, were misclassified into water areas because of topographic effect (see Figure 9a and 9b). Case 1 was compared with all other cases in the following discussion.

For case 2, even though most of the classification errors caused by topographic effect were corrected, major misclassification occurred at the borders of the water areas. Regions at the boundary of water areas were not classified into water areas because of discontinuity of texture values in edges as shown in Figure 5b and 5c. This caused overall underestimation of the water area over the study area.

The resulting classification image of case 3 showed that most of the misclassification in high relief areas located in the northwestern part of the study area was corrected. However, as shown in region *C* in Figure 8b and Figure 9c the classification errors were not completely removed in the severe steep areas due to shadow effects. This case presented a slight improvement in classification results, but required complicated calculation time and substantial efforts to remove the topographic effect.

In case 4 where the RADARSAT-1 SAR image was combined with the DEM, the classification accuracy was greatly improved in the flat areas and steep areas of the northwestern section. The result, however, failed to classify water areas in high
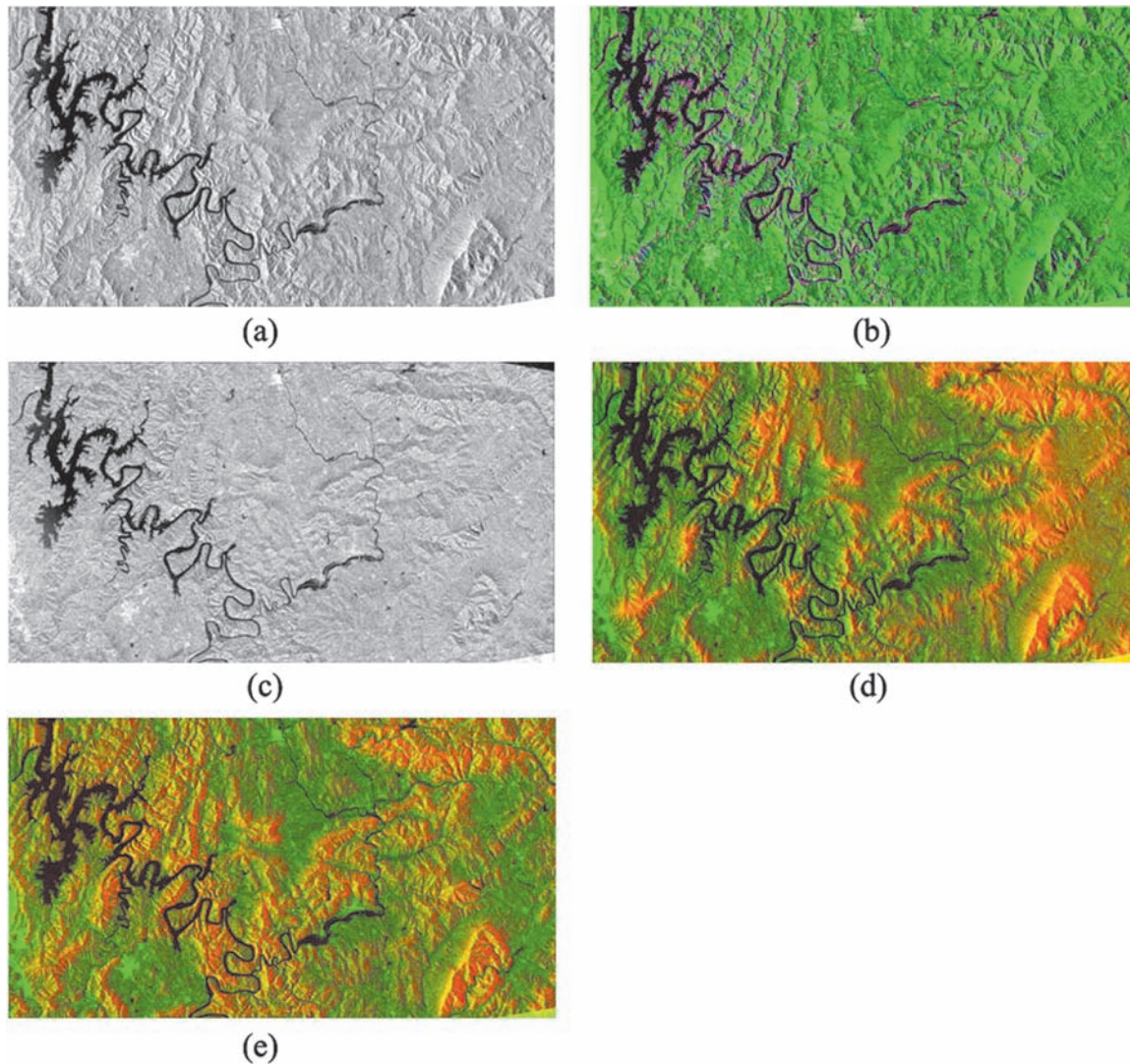
Plate 1. Processed RADARSAT images for classification: (a) only preprocessed image, (b) the combination image of three texture measures, (c) preprocessed and radiometric slope corrected image, (d) preprocessed image with DEM, and (e) preprocessed image with DSM.

TABLE 1. CHARACTERISTICS OF TRAINING SITE

	Water Area				Non-water Area			
	Min.	Max.	Mean	Std.	Min.	Max.	Mean	Std.
Back. coeff. (dB)	−23.95	−5.80	−19.71	1.60	−21.34	7.39	−8.30	3.56
Elevation (m)	39.24	145.16	72.52	14.76	105.00	929.27	324.85	200.72
Slope (degree)	0.00	11.34	0.43	0.91	0.00	39.56	10.31	9.99
GLCM								
Mean	0	255	15.37	27.16	0	255	44.05	50.43
Contrast	0	193	21.09	17.45	19	255	164.85	38.75
Variance	0	255	13.22	22.53	0	255	41.46	49.87
Total Number of Samples	10191				47595			

elevation and steep areas such as the upper middle section, marked region *E* in Figure 8d. In case 4, even a significant amount of misclassification was corrected over the areas where topographic effects such as shadow areas were dominant, but high elevation water areas failed to be classified as water areas. This suggests that if a flash flood occurred over a relatively flat area, a DEM could significantly improve classification accuracy.

The classification result of case 5 in which the preprocessed RADARSAT-1 SAR image was combined with the DSM
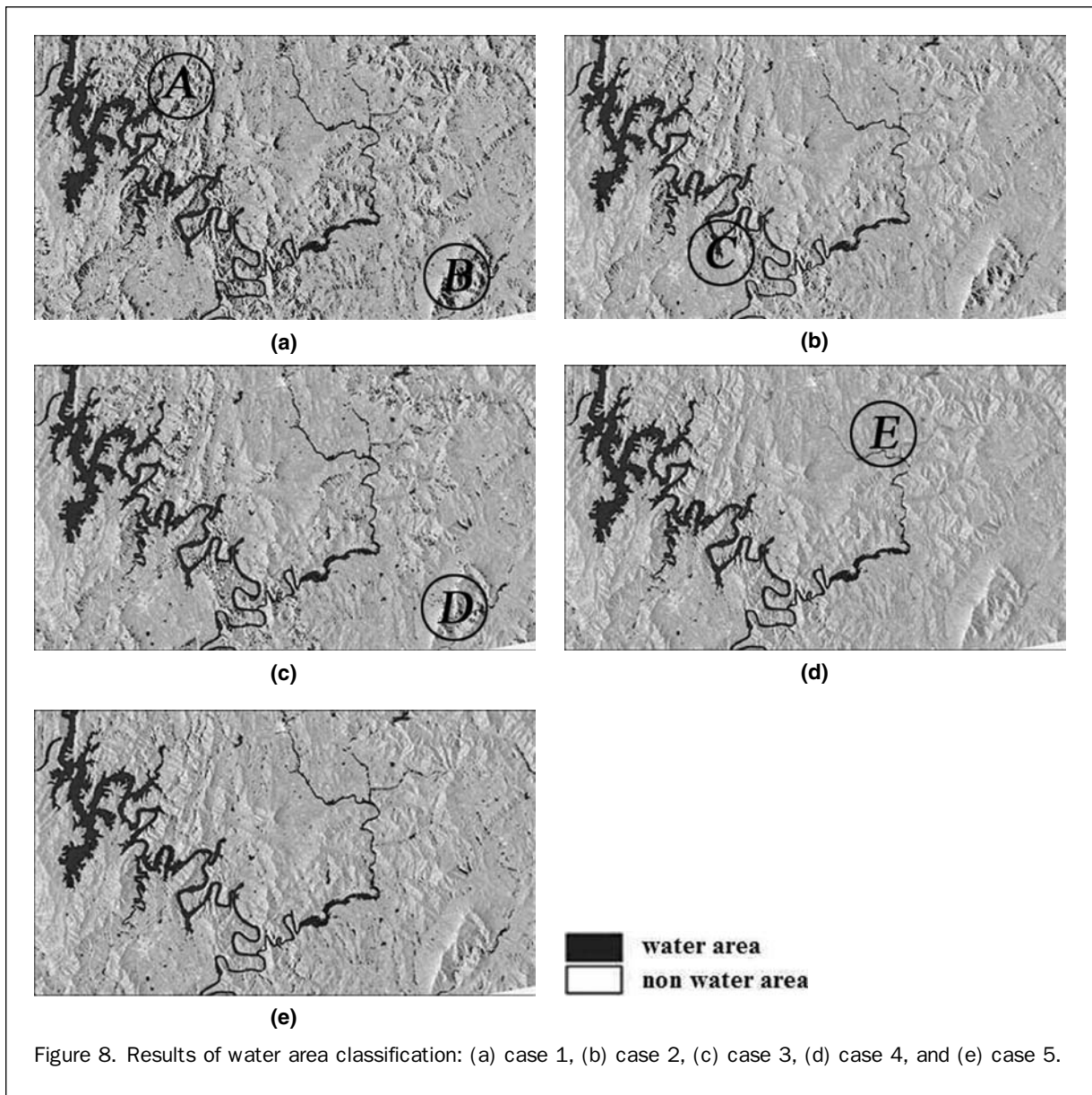
Figure 8. Results of water area classification: (a) case 1, (b) case 2, (c) case 3, (d) case 4, and (e) case 5.

TABLE 2. ACCURACY OF CLASSIFICATION RESULTS

	Producer Accuracy (%)		User Accuracy (%)			
	Water	Non-water	Water	Non-water	Overall Accuracy (%)	Kappa Cofficient
Case 1	99.25	96.02	86.54	99.80	96.67	0.90
Case 2	88.43	98.90	95.40	97.07	96.75	0.89
Case 3	97.73	97.02	89.42	99.40	97.16	0.91
Case 4	96.20	99.88	99.50	99.03	99.12	0.97
Case 5	98.20	99.66	99.54	98.68	99.36	0.98

exhibited the best performance (Figure 8e). This case not only classified correctly the areas where shadow effect was dominant, it also greatly improved the water area existed on high elevation and steep areas. Even though the result of case 5 is visually similar to that of case 3, case 5 has two distinct advantages over case 2. First, a DSM is easier to produce than the radiometric slope correction in which a complicated process needs to be performed. Second, the amount of processing time required by case 5 is much less than that of case 3. Since the DEM is usually available for SAR geometric correction, DSM can be easily reproduced out of the same DEM.

For more accurate assessment of the result, we introduced a diagram that represented the water area extraction ratio based on the slope. As shown in Equation 8, R_{S_i} refers to the water extraction ratio between the number of pixels with slope S_i classified into water areas and the number of pixels with slope S_i. The water extraction ratios were calculated over the entire classified images of each case:

$$R_{s_i} = \frac{\text{number of pixels with slope } S_i \text{ classified into water area}}{\text{total number of pixels with slope } S_i}$$

(8)

Figure 10 illustrates the plot of water extraction ratio versus local slope. The upper plot, in which the slope ranges from 0° to 3°, is the enlarged portion of the lower plot. The
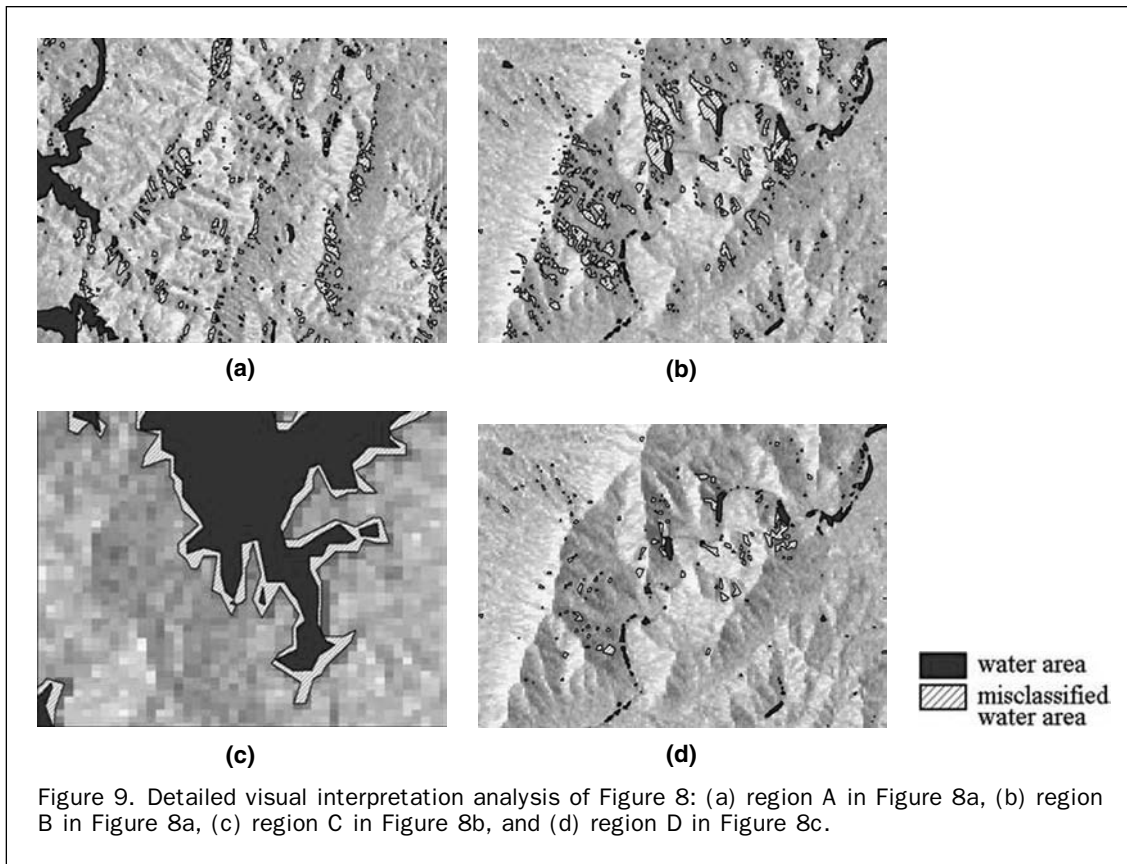
Figure 9. Detailed visual interpretation analysis of Figure 8: (a) region A in Figure 8a, (b) region B in Figure 8a, (c) region C in Figure 8b, and (d) region D in Figure 8c.
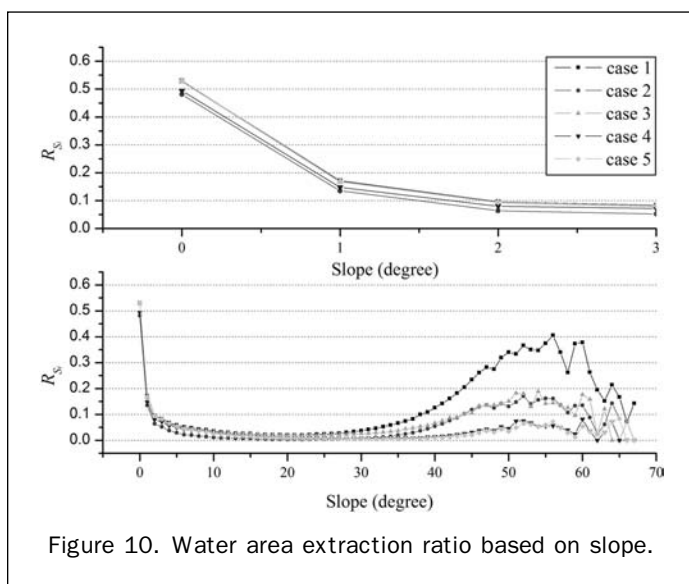

Figure 10. Water area extraction ratio based on slope.

slope information was obtained from the previous DSM. Based on the water extraction ratio, it can be hypothesized that the lower the slope, the higher the probabilities of water area become and the higher the slope, the lower the probabilities of water become. As shown in Figure 11, for all five cases the water extraction ratio gradually decreases about from 0° to 24°, but the patterns vary over 30° for each case.

Assessment of accuracy is based on our above-mentioned hypothesis. For lower slopes, which range from 0° to 30°, case 1 and case 5 are the best candidate approach, including most candidate pixels of the water area. For slopes higher than 40°, case 1 shows the worst results due to topographic effect of high relief. On the other hand, case 5 fits best with the hypothesis on the high slope areas. Based on the error matrix, visual interpretations, and the water extraction ratio analysis, we concluded that case 5 is the most appropriate method for classifying water areas in mountainous regions.

Additional study was performed to estimate the flooded area based on the water area extracted from RADARSAT-1 SAR image using the proposed method of case 5. For this, the raster format of the classified water area in case 5 was converted into vector format. The converted vector data was overlaid with the land-use map to verity the flooded areas and their land use. The land-use map was compiled at KNGII using ground survey, aerial photos, and satellite imagery. Figure 11 represents the portion of the flooded areas map generated from Figure 5e along the main river of the study area. In Figure 11, majority of the flooded areas were agricultural land while the area was 1.765 km^2. The flood caused additional damage of 0.193 km^2 to forestry, roads, and residential areas.

Conclusions

SAR images comprise a valuable tool for analyzing and monitoring a flood with cloud penetration capability and with the distinctive radar response of water surface. The classification of water area on flat regions is less problematic due to less radiometric and geometric distortions. On relatively flat areas, basic SAR processing techniques such as antenna pattern compensation, speckle noise reduction, and accurate geometric correction may be sufficient to compensate for the distortions to delineate water areas. In high relief mountainous area, however, local terrain relief, which causes severe radiometric distortions on the SAR image and
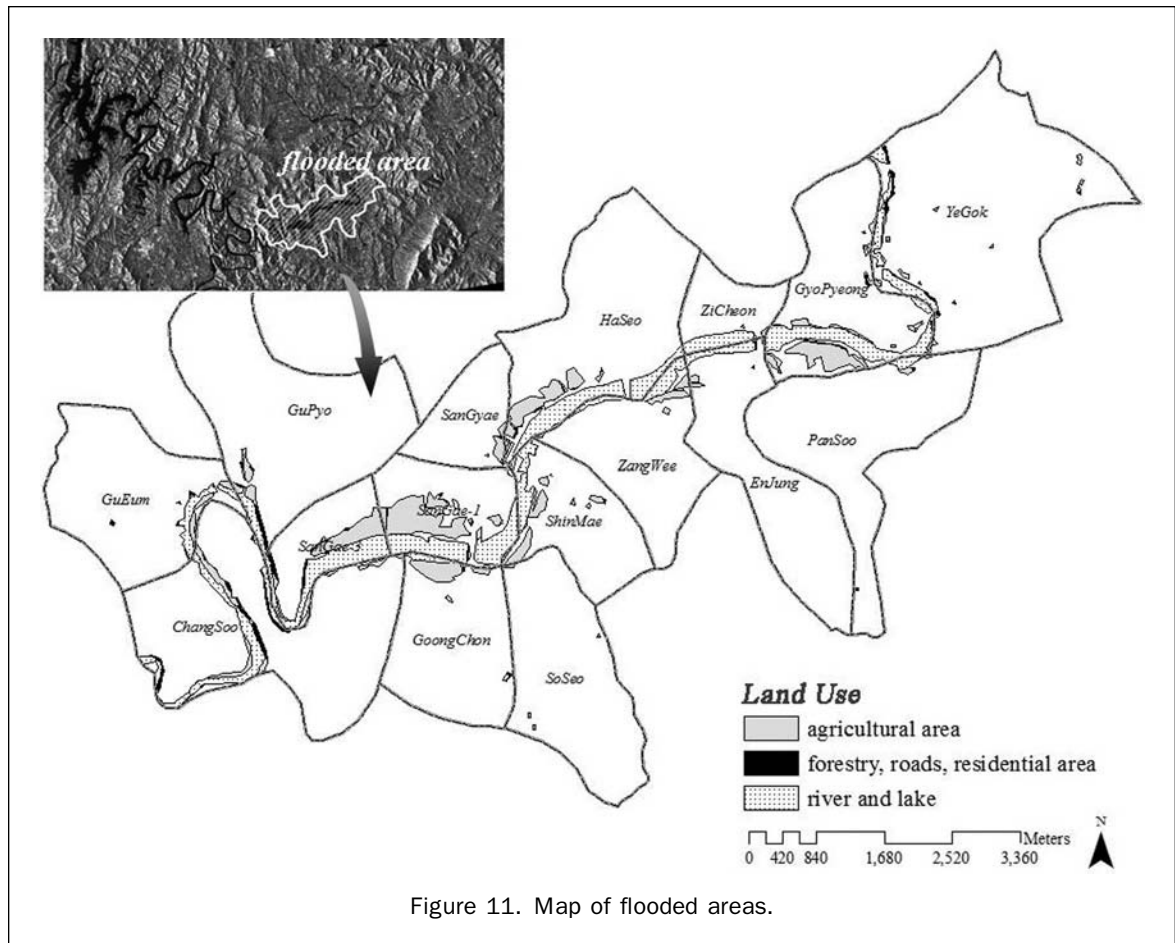
Figure 11. Map of flooded areas.

the fact that removing them requires considerable time and effort, must be carefully considered.

In this study five different cases based on RADARSAT-1 SAR image, GLCM texture measures, and additional terrain information (DEM and DSM) were investigated for efficient and accurate water area classification during a flood in a high relief mountainous environment. Among them, the DSM-based classification method emerged as the best choice for extracting water areas from a SAR image. The method provides promising results in both time efficiency and improving accuracy. However, the MIN filter needs to be applied to the DSM for better classification results during a flood, and the window size of the MIN filter and the number of iterations proved to be very critical factors affecting the result.

References

Alsdorf, D.E., L.C. Smith, and J.M. Melack, 2001. Amazon flood-plain water level changes measured with interferometric SIR-C radar, *IEEE Transactions on Geoscience and Remote Sensing*, 39(2):423–431.

Arzandeh, S., and J. Wang, 2002. Texture evaluation of RADARSAT imagery for wetland mapping, *Canadian Journal of Remote Sensing*, 28(5):653–666.

Aschbacher, J., P. Tiangco, C.P. Giri, R.S. Ofren, D.R. Paudyal, and Y.K. Ang, 1995. Comparison of different sensors and analysis techniques for tropical mangrove forest mapping, *Proceedings of IEEE-IGARSS'95*, 10–14 July, Florence, Italy, 3:2109–2111.

Bernier, M., Y. Gaunthier, P. Briand, J. Coulombe-Simoneau, J. Hurley, and F. Weber, 2002. Radiometric correction of RADARSAT-1 images for mapping the snow water equivalent (SWE) in a mountainous environment, *Proceedings of IEEE-IGARSS'02*, 24–28 June, Toronto, Ontario, 1:227–230.

Birkett, C.M., 1999. Synergistic remote sensing of Lake Chad: Variability of basin inundation, *Remote Sensing of Environment*, 72:218–236.

Brakenridge, G.R., T.T. Tracy, and J.C. Knox, 1998. Orbital SAR remote sensing of a river flood wave, *International Journal of Remote Sensing*, 19(7):1439–1445.

Costa, M., P.F., 2004. Use of SAR satellites for mapping zonation of vegetation communities in the Amazon floodplain, *International Journal of Remote Sensing*, 25(10):1817–1835.

Culander, J.C., 1984. Utilization of SAR data for mapping, *IEEE Transactions on Geoscience and Remote Sensing*, GE-22: 106–112.

Giacomelli, A., M.M. Mancini, and R. Rosso, 1995. Assessment of flooded areas from ERS-1 PRI data: An application to the 1994 flood in northern Italy, *Physics and Chemistry of the Earth*, 20(5–6):469–474.

Giesen, N.V.D., 2000. Characterization of west African shallow flood plains with L- and C-band radar, *Proceedings of Remote Sensing and Hydrology 2000 Symposium*, 02–08 April, Santa Fe, New Mexico, 267:365–367.

Goering, D.J., H. Chen, L.D. Hinzman, and D.L. Kane, 1995. Removal of terrain effects from SAR satellite imagery of Arctic tundra, *IEEE Transactions on Geoscience and Remote Sensing*, 33(1): 185–194.

Goyal, S.K., M.S. Seyfried, and P.E. O'Neill, 1998. Effect of digital elevation model resolution on topographic correction of

airborne SAR, *International Journal of Remote Sensing*, 19(3): 3076–3096.

Haralick, R.M., K. Shanmugam, and I. Dinstein, 1973. Textural features for image classification, *IEEE Transactions on Systems, Man, and Cybernetics*, 3(6):610–621.

Hess, L.L., J.M. Melack, S. Filoso, and Y. Wang, 1995. Delineation of inundated area and vegetation along the Amazon floodplain with the SIR-C synthetic aperture radar, *IEEE Transactions on Geoscience and Remote Sensing*, 33(4):896–903.

Holecz, F., A. Freeman, and J.J. van Zyl, 1995. Topographic effects on the antenna gain pattern correction, *Proceedings of IEEE-IGARSS'95*, 10–14 July, Florence, Italy, Vol. 1, pp. 587–589.

Horritt, M.S., D.C. Mason, D.M. Cobby, I.J. Davenport, and P.D. Bates, 2002. Waterline mapping in flooded vegetation from airborne SAR imagery, *Remote Sensing of Environment*, 85:271–281.

Imhoff, M.L., and C. Vermillion, 1987. Monsoon flood boundary delineation and damage assessment using space borne imaging radar and Landsat data, *Photogrammetric Engineering & Remote Sensing*, 53(4):405–413.

Kurvonen, L., and M.T. Hallikainen, 1999. Textural information of multitemporal ERS-1 and JERS-1 SAR images with applications to land and forest type classification in boreal zone, *IEEE Transactions on Geoscience and Remote Sensing*, 37(2): 680–689.

Lee, J.S., 1981. Speckle analysis and smoothing of synthetic aperture radar images, *Computer Graphics and Image Processing*, 17(1): 24–32.

Liu, Z., F. Huang, L. Li, and E. Wan, 2002. Dynamic monitoring and damage evaluation of flood in north-west Jilin with remote sensing, *International Journal of Remote Sensing*, 23(18): 3669–3679.

Marceau, D.J., P.J. Howarth, J.M. Dubois, and D.J. Gratton, 1990. Evaluation of the grey-level co-occurrence matrix for land cover classification using SPOT imagery, *IEEE Transactions on Geoscience and Remote Sensing*, 28(4):513–519.

Miranda, F.P., and L.E.N. Fonseca, 1998. Semiveriagram textural classification of JER-1 (Fuyo-1) SAR data obtained over a flooded area of the Amazon rainforest, *International Journal of Remote Sensing*, 19(3):549–556.

Mline, A., K.G. Horn, and M. Finlayson, 2000. Monitoring wetlands inundation patterns using RADARSAT multi-temporal data, *Canadian Journal of Remote Sensing*, 26(2):133–141.

Peng, X., J. Wang, M. Raed, and J. Gari, 2003. Land cover mapping from RADARSAT stereo images in a mountainous area of southern Argentina, *Canadian Journal of Remote Sensing*, 29(1):75–87.

Pope, K.O., E. Rejmankova, J.F. Paris, and R. Woodruff, 1997. Detecting seasonal flooding cycles in marshes of the Yucatan Peninsula with SIR-C polarimetric radar imagery, *Remote Sensing of Environment*, 59:157–166.

Pultz, T.J., and R.J. Brown, 1987. SAR image classification of agricultural targets using first- and second-order statistics, *Canadian Journal of Remote Sensing*, 13(2):86–91

Rauste, Y., 1989. Methods for analyzing SAR images, *Proceedings of the 9th EARSeL Symposium*, Espoo, Finland, 27 June–01 July, pp. 400–405.

Shang, J., 1996. *Evaluation of Multi-spectral Scanner and Radar Satellite Data for Wetland Detection and Classification in the Great Lakes Basin*, Masters thesis, University of Windsor, Ontario, 56 p.

Sheng, Y., and Z. Xia, 1996. A comprehensive evaluation of filters for radar speckle suppression, *Proceedings of IGARSS '96*, 21–26 May, Lincoln, Nebraska, 3:1559–1561.

Sohn, H.G., Y.S. Song, and G.H. Kim, 2005, Radargrammetry for DEM generation using minimal control points, *Proceedings of IEEE-IGARSS'2005*, 25–29 July, Seoul, Korea, unpaginated CD-ROM.

Sokol, J., T. Pultz, and V. Bulzgis, 2000. Investigating Labrador fens and bogs using multi-temporal ERS-2 and RADARSAT data, *Proceedings of the 22nd Annual Canadian Remote Sensing Symposium*, 21–24 August, Victoria, B.C., Ontario, pp. 357–364.

Sun, G., K.J. Ranson, and V.I. Kharuk, 2001. Radiometric slope correction for forest biomass estimation from SAR data in the western Sayani Mountains, Siberia, *Remote Sensing of Environment*, 79:279–287.

Teillet, P.M., B. Guindon, J.F. Meunier, and D.G. Goodenough, 1985. Slope aspect effects in synthetic aperture radar imagery, *Canadian Journal of Remote Sensing*, 11:39–50.

Townsend, P.A., 2001. Mapping seasonal flooding in forested wetlands using multi-temporal RADARSAT SAR, *Photogrammetric Engineering & Remote Sensing*, 67(7):857–864.

Treitz, P.M., and P.J. Howarth, 2000. Integrating spectral, spatial, and terrain variables for forest ecosystem classification, *Photogrammetric Engineering & Remote Sensing*, 66(3):305–317.

Treitz, P.M., P.J. Howarth, O.R. Filho, and E.D. Soulis, 2000. Agricultural crop classification using SAR tone and texture statistics, *Canadian Journal of Remote Sensing*, 26(2): 18–29.

Töyrä, J., A. Pietroniro, L.W. Maritz, and T.D. Prowse, 2002. A multi-sensor approach to wetland flood monitoring, *Hydrological Process*, 16:1569–1581.

Ulaby, F.T., F. Kouyate, B. Brisco, and T.H.L. Williams, 1986. Textural information in SAR images, *IEEE Transactions on Geoscience and Remote Sensing*, 24(2):235–245.

Ulander, M.H., 1996. Radiometric slope correction of synthetic-aperture radar images, *IEEE Transactions on Geoscience and Remote Sensing*, GE-34(5):1115–1122.

van Zyl, J.J., B.D. Campion, P. Dubios, and J. Shi, 1993. The effect of topography on SAR calibration, *IEEE Transactions on Geoscience and Remote Sensing*, GE-31(5):1036–1043.

Wang, J., J. Shang., B. Brisco, and R.J. Brown, 1998. Evaluation of multidate ERS-1 and multispectral Landsat imagery for wetland detection in southern Ontario, *Canadian Journal of Remote Sensing*, 24(1):60–68

Wickel, A.J., and T.J. Jackson, 2001. Multitemporal monitoring of soil moisture with RADARSAT SAR during the 1997 southern great plain hydrology experiment, *International Journal of Remote Sensing*, 22(8):1571–1583.

Zaman, M.R., and C.R. Moloney, 1993. A comparison of adaptive filters for edge-preserving smoothing speckle noise, *Proceedings of ICASSP'93*, 27–30 April, Minneapolis, Minnesota, 5:77–80.